Nuclear Materials and Energy 45 (2025) 101990

Contents lists available at ScienceDirect

Nuclear Materials and Energy

journal homepage: www.elsevier.com/locate/nme

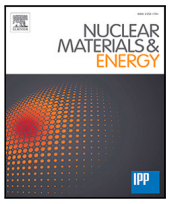

Influence of redeposited tungsten and EUROFER97 layers on deuterium retention in plasma-facing materials☆

Martina Fellinger [a,*], Eduardo Pitthan [b], Daniel Gautam [b], Daniel Primetzhofer [b], Friedrich Aumayr [a]

[a] Institute of Applied Physics, TU Wien, Fusion@ÖAW, Wiedner Hauptstraße 8-10/E134, 1040 Wien, Austria
[b] Department of Physics and Astronomy, Uppsala University, Box 516, 75120 Uppsala, Sweden

ARTICLE INFO

Keywords:
Retention
Fuel trapping
Plasma facing materials
Redeposition

ABSTRACT

Retention of hydrogen isotopes in plasma-facing materials is a key challenge for safety and fuel efficiency of nuclear fusion reactors. In realistic reactor environments, simultaneous processes, such as erosion, redeposition, implantation and outgassing, can alter surface compositions and may affect hydrogen isotope retention. In this study, we investigate how thin redeposited layers of tungsten and EUROFER97 influence retention and release of previously implanted deuterium. Using a combination of Elastic Recoil Detection Analysis and Rutherford Backscattering Spectrometry, we quantify deuterium retention during in-situ annealing up to 600 °C. Comparisons between coated and uncoated samples show that redeposited tungsten can act as partial diffusion barrier, preventing deuterium from outgassing. In contrast, redeposited EUROFER97 layers show no such effect and appear virtually transparent to deuterium diffusion. These findings emphasize the critical role of redeposited layers on fuel retention and have implications for wall lifetime estimates and fuel inventory control in fusion devices.

1. Introduction

Hydrogen isotope retention in the first wall of nuclear fusion devices has crucial implications. Firstly, the capture of fusion fuel directly limits the reactor efficiency [1,2]. Secondly, when using tritium (T) as fusion fuel, trapping in the plasma-facing material (PFM) raises important safety concerns due to its radioactivity [3,4]. Additionally, hydrogen isotope retention can lead to chemically assisted sputtering, as observed for the case of beryllium (Be) [5] and tungsten (W) [6]. While macroscopic retention in operational devices can be quantified using post-mortem analysis [7] or global gas balance [8], laboratory experiments remain essential to understand the underlying microscopic mechanisms [9–11] and to investigate how fundamental properties [12,13], different production techniques or pretreatment [14–16] influence retention.

In addition to its fundamental relevance, retention must also be considered in the context of the highly dynamic plasma-wall-interaction processes, occurring in fusion reactor environments. Particle impingement in a reactor environment can lead to damage in material layers, affecting its properties [17–21]. In operating devices, PFMs are subject to continuous erosion and redeposition, in parallel with implantation and outgassing. These processes can furthermore lead to the formation of complex, layered structures. Redeposited layers may substantially modify the retention behavior compared to pristine surfaces. Investigations of the full interplay of all processes are solely feasible within a reactor device. However, to enable predictions as well as to allow improved design solutions for future machines, it is necessary to investigate and disentangle potential synergistic effects within laboratory experiments. Thus, this study aims to investigate the possible interplay between redeposition of thin material layers and retention of fusion fuel.

The primary candidates for armor and structural material in DEMO are W and EUROFER97 [22,23], which is why we investigated these two plasma facing material candidates and furthermore used deuterium (D) as representative projectile species for the retention studies. Redeposited layers were grown ex-situ via magnetron sputter deposition. Using Ion Beam Analysis (IBA) techniques, we quantified the amount of D retained in different W and EUROFER97 layer systems during in-situ annealing. Bare D-loaded layers without additional coating were also studied as reference samples. By comparing the outgassing characteristics of D-implanted bare materials to D-implanted coated layer systems, we simulate possible redeposition scenarios and assess their impact on D retention and release behavior in a reactor environment.

☆ This article is part of a Special issue entitled: 'PFMC-20' published in Nuclear Materials and Energy.

* Corresponding author.
E-mail address: fellinger@iap.tuwien.ac.at (M. Fellinger).

https://doi.org/10.1016/j.nme.2025.101990
Received 30 June 2025; Received in revised form 16 August 2025; Accepted 15 September 2025
Available online 20 September 2025

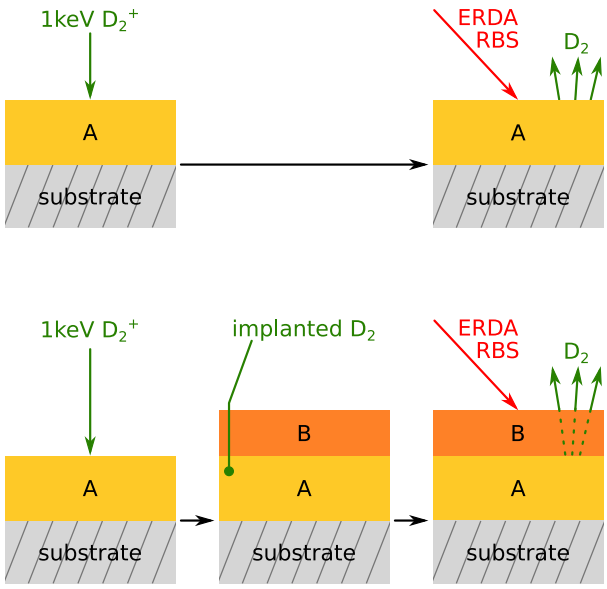

Fig. 1. Visualization of the measurement procedure containing individual steps: Implantation, coating and annealing. This series of measurement steps was conducted twice: for the case of A = W and B = EUROFER97 and for the inverted case of A = EUROFER97 and B = W.

2. Experimental procedure and characterization

2.1. Measurement procedure

To investigate possible synergistic effects between retention and re-deposition, we employed a systematic measurement procedure, which is presented in this section. Fig. 1 shows an illustration of the performed procedure. As sketched in Fig. 1, the primary material layer, labeled A, was initially irradiated by D ions. This implantation step was performed on a single sample, which was subsequently separated into two sample halves with the same nominally implanted fluence. The sample separation was realized by manually braking the sample into two parts. The sample consisted of the coating layer on top of a gold (Au) coated silicon dioxide (SiO_2) substrate of 0.3 mm in thickness (further details on the composition of the coating and the sample sandwich structure are given in Sections 2.2 and 2.4). Due to the low sample thickness and the resulting fragility and comparably easy breakability, we consider influences caused by breaking, such as significant local heating, to be unlikely. One sample half was subsequently coated ex-situ with a thin material layer, labeled B in Fig. 1. The other sample piece remained uncoated but underwent the same ex-situ handling in order to ensure comparable conditions between the two sample pieces. Finally, both sample halves were subjected to individual annealing ramps up to approximately 600 °C. During annealing in-situ IBA techniques, specifically Rutherford Backscattering Spectrometry (RBS) and simultaneous Elastic Recoil Detection Analysis (ERDA) were performed to quantify the D content in the sample. These measurement steps were performed twice: once with W as base (layer A) and EUROFER97 as top layer (layer B), and once with EUROFER97 as base (layer A) and W as top layer (layer B), essentially representing inverted layer structures.

Each experimental step, i.e. sample preparation and pre-characterization, implantation, coating and annealing are described in more detail, in the following subsections.

2.2. Sample preparation and pre-characterization

The initial layers (labeled A in Fig. 1) were created using a magnetron sputter device [24]. The base pressure was in the range of 4×10^{-7} mbar and depositions were carried out in Ar atmosphere using a gas flow rate of 10 standard cubic centimeter per minute, Ar pressure of 5.5×10^{-3} mbar, and a DC power of 50 W. The growth of the W layer was achieved by simply installing a W target into the magnetron sputtering device, while a previously successfully developed procedure enabled us to deposit layers from EUROFER97 with comparable composition [25]. Layers of 150–300 nm in thickness were grown on Au coated SiO_2 substrates. Reference layers for characterization purposes were created in the same growth run on Si substrates.

Prior to further measurements, the purity of the grown reference layers on Si was investigated ex-situ by Time-of-Flight Elastic Recoil Detection Analysis (ToF-ERDA) using 36 MeV I^{8+} ions for the probing beam [26]. The elemental profiles obtained by the ToF-ERDA measurements are shown in Fig. 2. Panel (a) shows the W layer, while the EUROFER97 coating is shown in Fig. 2 (b). In both cases, surface contamination by mainly oxygen (O), was observed, with higher levels for EUROFER97 (b), compared to W (a). However, this surface contamination decreased rapidly within the subsequent material depth. The bulk composition showed high purity in the W case. The EUROFER97 coating, consisting of mainly iron (Fe) and additional alloy components including chromium (Cr) and W, was confirmed to have comparable composition to bulk EUROFER97 [25]. For reference, an additional x-axis, shown on top of the plots, indicates the physical depth in nm. This is an estimated depth, when assuming W or Fe bulk density for W and EUROFER97, respectively. The measured quantity in 10^{15} at/cm^2 is shown on the bottom x-axis.

2.3. Implantation

D implantation was performed by using a Prevac IS40 ion source, capable of producing and accelerating D ions. We used an acceleration voltage of 1 keV, yielding 93% 1 keV D_2^+ ions and 7% 1 keV D^+ ions [27], and irradiated the sample at normal incidence. It can be stated that molecular ions dissociate into atomic particles upon surface impact. The two D particles then perform individual collision cascades within the material. Each D atom is assumed to carry half of the initial energy, i.e. 500 eV, since the chemical binding energy of the D_2 molecule is negligible compared to the kinetic energy of 1 keV [28]. To estimate the implantation depth of both 1 keV D and 500 eV D particles, the collision was simulated using the binary-collision-approximation code SDTrimSP [29], employing a user-friendly graphical user interface [30]. The calculated implantation profiles, shown in Fig. 3, indicate shallow implantation depths, below approximately 30 nm, for both W and EUROFER97.

Ion fluxes during implantation were approximately 10^{17} ions/m^2/s. The implantation steps were performed for approximately 20 h, resulting in a nominally implanted fluence of approximately 10^{22} ions/m^2. No intentional heating was performed and the temperature of the sample was neither controlled nor monitored during the implantation step.

2.4. Coating

The coating step was again performed via magnetron sputtering. No intentional heating was performed and sample temperatures during the coating step were neither controlled nor monitored. The initial layers (labeled A in Fig. 1) were coated with a coating layer (layer B in Fig. 1) resulting in a final sample sandwich: layer B on layer A on Au coated SiO_2 substrate. Reference layers of layer B were again grown on Si substrates for characterization purpose. For this coating procedure, the samples were handled ex-situ for a few hours. In order to reach comparable conditions between the coated and the non-coated samples, the non-coated ones were transported ex-situ as well. The grown layers were characterized by ToF-ERDA by using 36 MeV I^{8+} ions for the probing beam. To approximate redeposition layers that could potentially form under reactor-relevant conditions, we aimed for layer

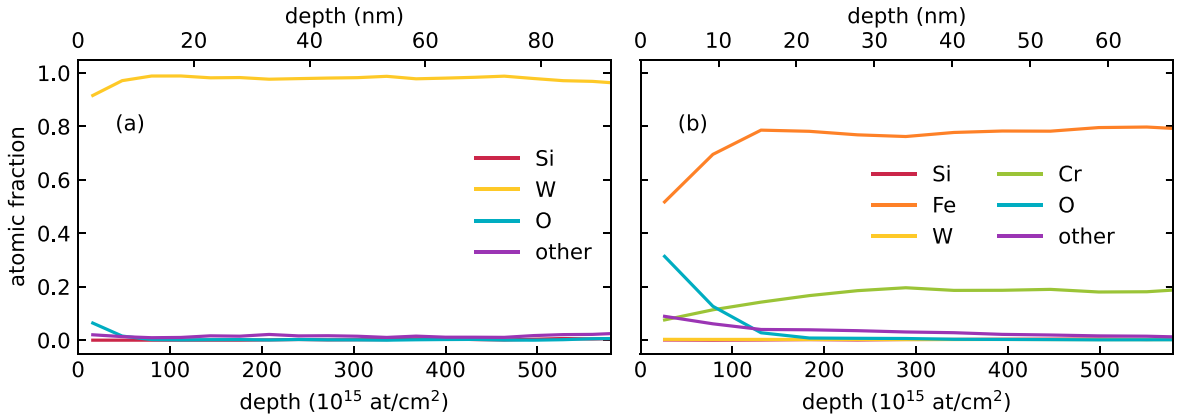

Fig. 2. Composition depth profiles of (a) the as-deposited W layer and (b) the as-deposited EUROFER97 layer obtained by ToF-ERDA. Measured depth values in terms of 10^{15} at/cm^2 are given on the bottom x-axis. The top x-axis shows the depth in nm when assuming (a) bulk W or (b) bulk Fe density.

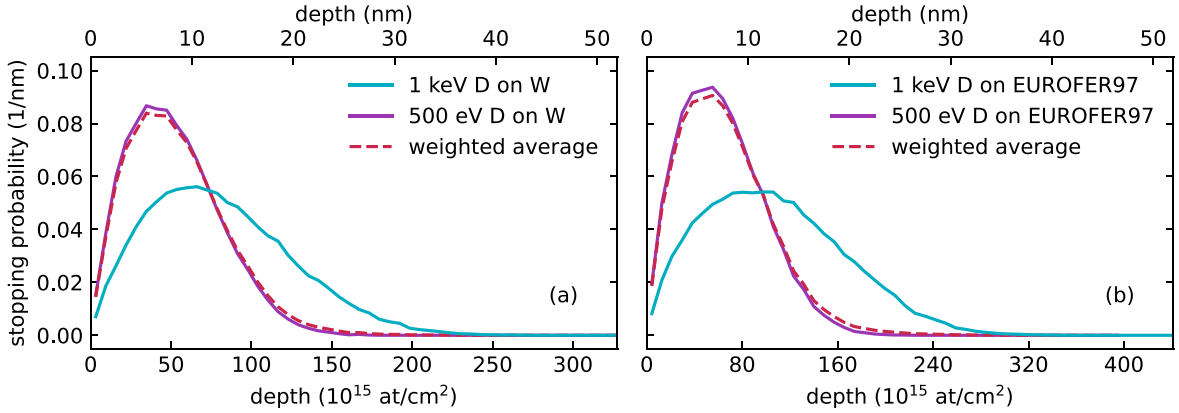

Fig. 3. Implantation profiles of 1 keV D and 500 eV D particles in (a) W and (b) EUROFER97. A weighted average of the two contributions, i.e. 93% 500 eV D and 7% 1 keV D is shown by the dashed magenta colored line. Simulated depth values in nm are given on the top x-axis. The bottom x-axis shows the depth in 10^{15} at/cm^2 when assuming (a) bulk W or (b) bulk Fe density.

thicknesses in the order of a few 10 nm [32]. Since ToF-ERDA reaches its resolution limits within this thickness regime, we additionally performed RBS on the final sandwich structure to accurately quantify the layer thicknesses. The obtained depth profiles from ToF-ERDA as well as the RBS spectra are visualized in Fig. 4. It should be noted that the ToF-ERDA measurements were performed on the reference coatings on Si substrates. Furthermore, it should be noted that for the W case, an additional slightly thicker layer was grown (same parameters but longer deposition time) in order to enable investigation of the bulk purity. Figs. 4 (a) and (b) show the ToF-ERDA profiles of the slightly thicker W and the EUROFER97 layer on Si substrates, respectively. Figs. 4 (c) and (d) show the obtained RBS spectra from the final sandwich structure, i.e. layer B on layer A on Au coated SiO_2 substrates.

From the elemental profiles shown in Figs. 4 (a) and (b), surface contamination could be identified. This contamination, primarily consisting of O, could have been caused during the layer growth itself or the ex-situ handling. Generally, it cannot be ruled out that such contamination may also have influenced the retention behavior. However, typical cleaning processes often rely on sample heating or erosion of the contamination layers. As heating would interfere with the subsequent annealing procedure and the small thickness of the redeposited layers investigated in this study (below 20 nm) limited the applicability of erosion-based cleaning methods, contamination removal remained challenging. In addition, possible oxidation in the reactor itself cannot be ruled out either, which rationalizes the investigation of the retention behavior of the grown layers without additional cleaning processes [33].

Furthermore, it should also be noted that the ToF-ERDA data did not show step-like elemental profiles. The substrate signal, in this case Si, largely overlapped with the signal of the coating layer. This effect was more pronounced in (a) the EUROFER97 case than in (b) the W case, which is attributable to the thinner EUROFER97 film (below 20 nm), while the W layer shown in (b) represents a slightly thicker layer. Such overlap between substrate and coating signals can give a misleading impression of the data. In addition to the fact that the depth resolution of ToF-ERDA is generally limited for our case, dual or multiple scattering effects, which can lead to systematic errors in the measurement methodology, can play a role. Such effects may lead to an apparent but nonphysical overlap of the signals as demonstrated by Pitthan et al. [34]. In contrast to the ToF-ERDA data, the RBS data shown in (c) and (d) do not indicate such an overlap. The measured RBS spectra could be reproduced by simulating the experiment via the simulation program SimNRA [31] and by utilizing an input layer structure as visualized in the plot inserts. Contributions of individual elements are shown, the sum of which corresponds well with the experimental spectrum. Thus, RBS provided accurate information on layer thicknesses, while ToF-ERDA allowed for the assessment of contamination and layer purity.

2.5. Annealing

During the annealing step, the retained amount of D inside the sample was monitored in real-time via IBA techniques. Additionally,

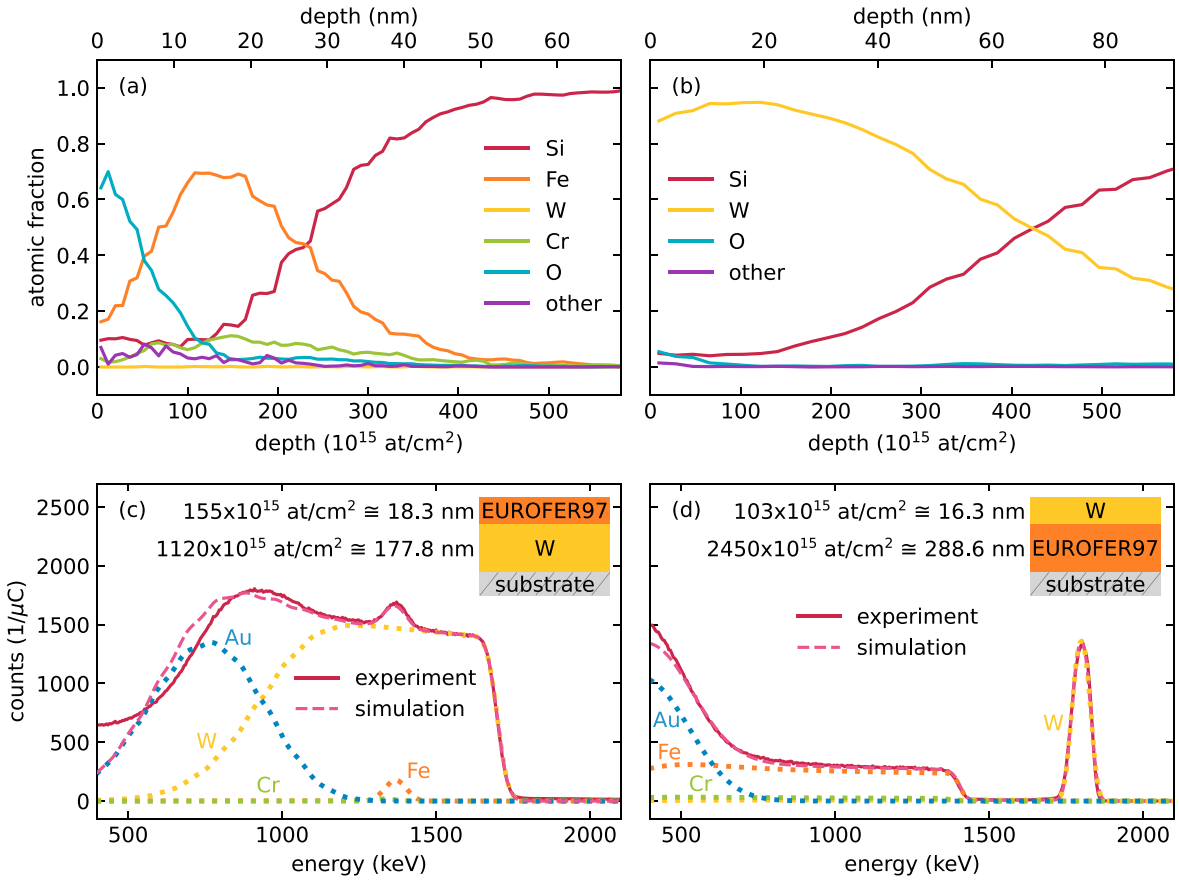

Fig. 4. Characterization of the coating layer: Elemental profiles of (a) the EUROFER97 coating layer and (b) the W coating layer, obtained by ToF-ERDA. (a) and (b) show data obtained from twin sample layers on Si substrates (not the sandwich structure). Measured depth values in terms of 10^{15} at/cm^2 are given on the bottom x-axis. The top x-axis shows the depth in nm assuming (a) bulk Fe or (b) bulk W density. RBS data of the full sandwich structure are visualized in panel (c) for the W + EUROFER97 structure and panel (d) for the EUROFER97 + W structure. Besides experimental spectra, panels (c) and (d) also show simulated RBS spectra (obtained via the simulation program SimNRA [31]) with contributions from different elements shown individually. The simulation input structure together with the thickness values is sketched via an insert on the top right of panels (c) and (d).

the content was monitored prior to the annealing phase and after the annealing phase. These measurements were performed analogously to the measurements during annealing but with higher statistical accuracy and will in the following be referred to as pre- and post-annealing phase.

The annealing measurements were performed under vacuum conditions of approximately 10^{-7} mbar (during annealing) to 10^{-8} mbar (pre- and post-annealing) at the Setup for In-Situ Growth, Material Modification and Analysis (SIGMA) at Uppsala University [27], which is connected to a 5-MV NEC-15SDH-2 Tandem accelerator [35]. A sketch of the setup, including the features that were utilized during this study, is shown in Fig. 5. The sketch visualizes the arrangement of the IBA detectors, i.e. the RBS detector, located at 170 ° scattering angle and the ERDA detector located at 30 ° scattering angle with respect to the primary beam direction. The primary beam of 2.13 MeV helium ions (He^+), is visualized as red arrow. In addition, the ion source (IS), which was used during the implantation step, described in Section 2.3, is shown. It should be noted that the D ion irradiation was performed perpendicular to the surface, meaning that the sample was rotated differently for the implantation step compared to the annealing step, which is indicated by the two different rotation angles of the sample in the sketch. During the annealing, the impinging ions were directed onto the sample under 65 ° incidence angle with respect to the surface normal to allow both detectors, ERDA and RBS, being used simultaneously. Furthermore, the visualization in Fig. 5 schematically shows the electron beam heating filament (EBHF), placed behind the sample, enabling the heating ramp. To achieve uniform heat distribution during annealing and to minimize detector noise from light emitted by the EBHF, a W foil of approximately 100 μm thickness, was placed between the sample holder, incorporating the EBHF, and the sample. However, despite this precaution, noise especially in lower channels could not be fully prevented.

Besides the location of the detectors, the sketch visualizes that the detectors were equipped with absorber-foils of a certain thickness. On the one hand, this additionally reduces noise in the detectors caused by light emitted from filaments. On the other hand, the thickness of the foil in front of the ERDA detector was chosen such that primary He particles are fully stopped within the foil and only lighter elements than He can penetrate through the foil. Thus, the resulting ERDA spectra consists solely of contributions from hydrogen (H) and D. Cutting off the scattered primary particles, however, poses a problem for quantification, making additional measurements necessary. To circumvent this problem, the RBS signal was used as a measure for the amount of incoming particles, which was utilized for quantification of the ERDA signal. All RBS and ERDA spectra were analyzed using the simulation program SimNRA [31].

The energy of the primary particles was chosen to utilize resonant cross section for the scattering of He on D. The resonant peak lies at 2.13 MeV with an approximate full width at half maximum (FWHM) of 70 keV [36]. Taking into account the stopping power of the primary 2.13 MeV He projectiles in W or Fe and the incidence angle of 65 °, 70 keV translates to an approximate thickness of around 50 nm, which allows for a probing depth comparable to the initial implantation depth. Nevertheless, we want to stress that due to this resonant peak the cross

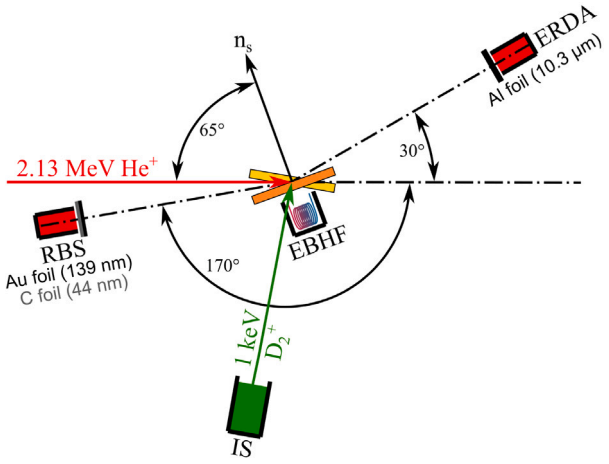

Fig. 5. Sketch of the utilized features of the SIGMA chamber at Uppsala University [27]: The primary beam of 2.13 MeV He^+ ions, a detector for Rutherford Backscattering Spectrometry (RBS), a detector for Elastic Recoil Detection Analysis (ERDA), an ion source (IS) and an Electron Beam Heating Filament (EBHF).

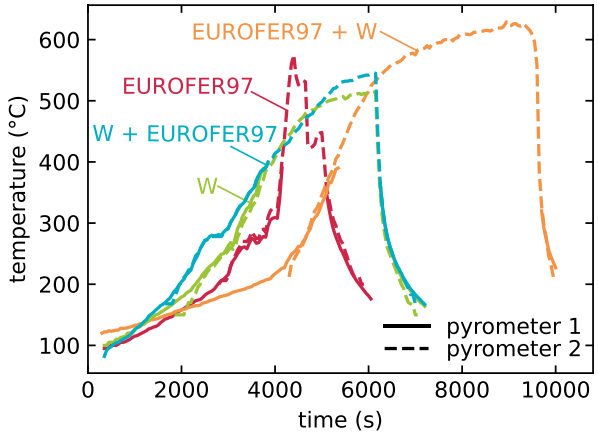

Fig. 6. Temperature ramps for each sample, monitored with two different pyrometers with different working temperatures, as shown by the dashed and solid lines.

section varies largely around the maximal value at the resonant energy. Thus, slight deviations from the resonance energy may drastically affect signal quantification due to the narrow FWHM (≈ 70 keV) of the cross section. This aspect will be addressed in more detail in the discussion of the results.

Each sample was heated to a maximum temperature of approximately 600 °C, as shown in Fig. 6. The temperature was monitored via two pyrometers with different operating temperatures. The data is marked with solid lines for the low temperature pyrometer and dashed lines for the high temperature pyrometer. At a temperature interval of approximately 200 °C–400 °C both pyrometers could be operated and showed good agreement. The temperature ramps were realized by manually increasing the applied voltage on the EBHF. Additionally, different filaments were used during the course of this study, which is why the individual ramps differentiate from each other. It cannot be excluded that the slightly different heating rates and different duration at maximum temperature, which resulted from technical limitations, influenced the retention behavior.

3. Results and discussion

Initial insight into the retention behavior can be obtained by comparing ERDA spectra acquired before and after annealing. These spectra are shown in Fig. 7 and consisted of two distinct peaks, corresponding to contributions of H and D. Heavier particles were stopped within the employed foils, as mentioned in Section 2.5.

Intensities of the peaks are directly related to the density of the scatterer. The energy of the recoils depends not only on the scatterer, but also on the depth, where the scattering process happens, due to attenuation in the material, and the energy loss of recoils in the foils in front of the detector. Thus, depth scales for both H and D are indicated in Fig. 7. The scale was set to 0 at the surface for each sample case. In the case of the layered structures EUROFER97 + W and W + EUROFER97 the depth values were counted individually for the different material layers starting from zero at both the surface and the interface. The material is indicated schematically in the depth scale bar by the respective colors (yellow representing W, orange representing EUROFER97).

The spectra presented in Fig. 7 compare experimental and simulated data for the four investigated cases. In the simulations surface-near regions (the topmost ≈ 40 nm) containing H and D were included to replicate the observed signal intensities. These surface-near regions essentially represent the implantation zones (see Fig. 3) and it is expected that most of the retained D sits within the surface-near layers. However, the observed peak shapes suggested also the presence of sub-surface H and D. We estimated these distributions by adding bulk contributions of H and D into the modeling. The presence of D in deeper layers may be attributed to diffused D originating from the implantation zone. The presence of H in both the near-surface region as well as the sub-surface region is attributed to residual contamination in the samples and the vacuum chamber. Despite the overall good agreement between the experimental spectra and the fit, discrepancies remained in the very low energy regime. Accurately reproducing this part of the spectrum was particularly challenging due to several compounding factors, including instrumental noise, potential non-linearity in the detector calibration, overlapping signals of H and D from deeper in the sample, surface and interface roughness, potential signals from residual primary ions and the strong influence of straggling effects on H and D recoil signals at these energies.

Qualitatively, both peak intensities, directly related to retained amounts of H and D, decreased as a result of the annealing process. Additionally, it is visible that in most cases the energy of the peaks remained constant before and after annealing, suggesting that H and D were released uniformly from the implanted region. An exception was observed for the EUROFER97 + W case, shown in Fig. 7 (d), where a slight shift in the D and H peak position occured. This shift points to changes in the depth distribution of retained D and H, discussed in more detail in Section 3.1.

Quantitative data could be derived from the simulated spectra, based on the layer configuration that yielded the best fit to the experimental spectra. The obtained values are shown in Fig. 8. Each bar represents the H or D content in the sample before annealing (labeled pre) or after the annealing (labeled post) for all investigated cases (a)–(d). The data only represent the retained amounts in the surface-near regions, i.e. the topmost ≈ 40 nm of the initially implanted layers plus the additional coating layer. The contributions from the individual layers are indicated by the shade in yellow (representing W) and orange (representing EUROFER97). Contributions from the bulk are not shown. The layer structure is shown as an insert on the top right of each panel. The following conclusions can be drawn from this analysis: The initial H content was significantly higher for the layered structures (c) and (d) compared to the uncoated cases (a) and (b), which can be attributed to the additional interface that was exposed to air for the layered structures. Comparing pre- and post- annealing contents, overall a decrease was found in each case. The smallest reduction was measured

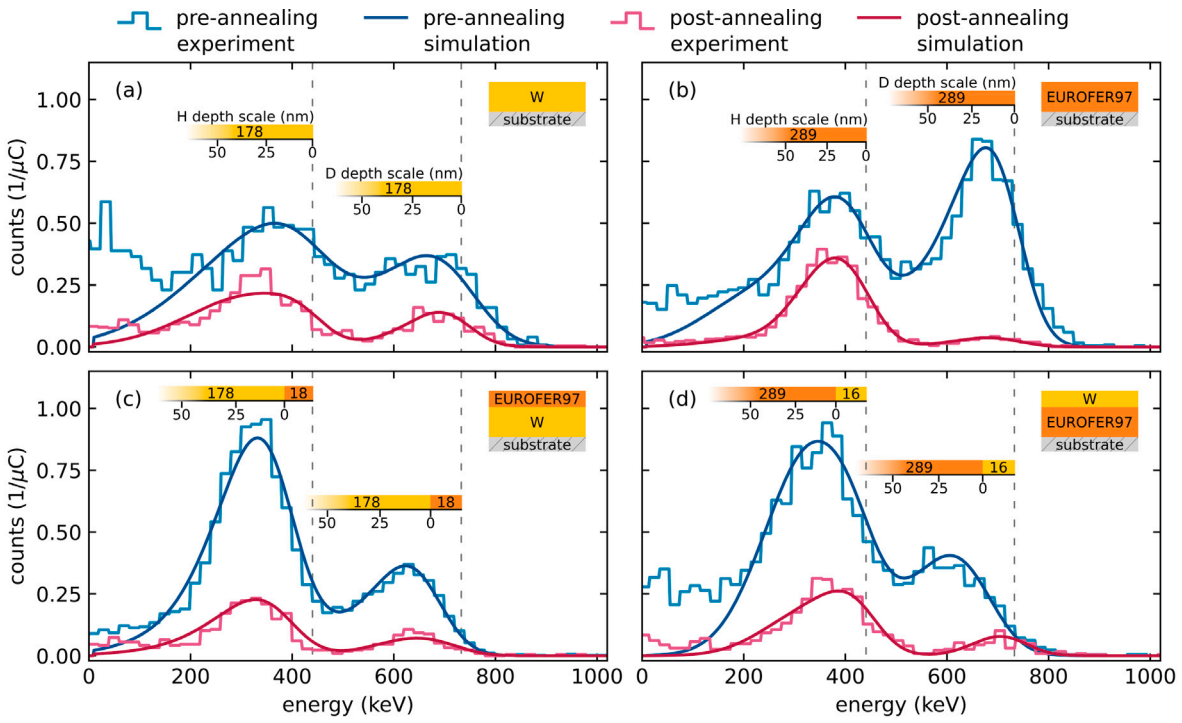

Fig. 7. Pre- and Post-Annealing ERDA spectra shown individually for all investigated layers. Depth scales for the detected recoils, H and D, are included above the spectra. The vertical dashed gray line indicates the surface position. Depth values from deeper in the sample were counted for the different material layers individually and are indicated by the scale bars and the shade. Total layer thicknesses are included in the color shades above the scale.

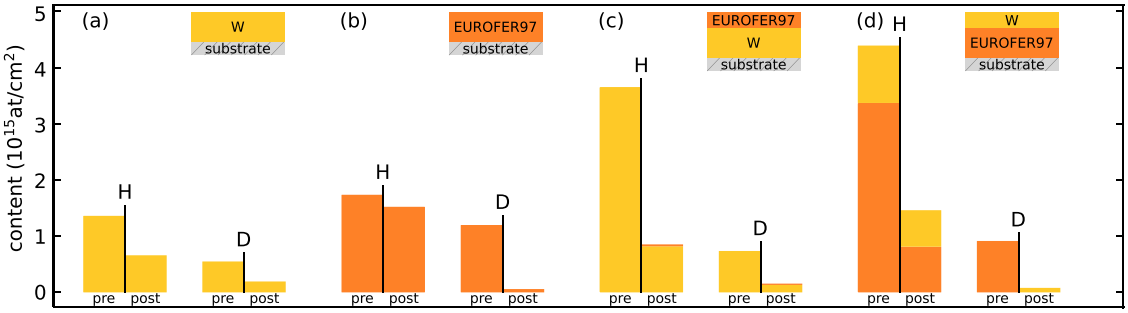

Fig. 8. Quantitative data on the retained H and D content before and after the annealing in the topmost ≈40 nm of the initially implanted and the additional coating layer. Contributions from the bulk are excluded. H is shown via the left two bars, D is shown via the right two bars in each grouped section representing the different sample cases (a)–(d). Contributions from individual layers are indicated by the shade in yellow (W) and orange (EUROFER97).

for H in the non-coated samples (a) and (b), while a significantly larger decrease was found for H in the sandwich-samples (c) and (d). This indicates that surface-bound H on the surface largely remained. While surface H was expected to desorb during annealing, it likely re-adsorbed during the subsequent cool-down. In contrast, interface H appeared to be effectively removed as a result of the annealing procedure. However, it should additionally be noted that isotope exchange processes during the ex-situ handling cannot be fully excluded either, but seem not to be significant, as the D contribution pre annealing is not substantially lower in the coated samples compared to the uncoated samples.

The D content, on the other hand, decreased substantially in both coated and non-coated samples as a result of annealing. This can be attributed to the lack of D in the environment post-annealing, making re-adsorption of D impossible.

Besides pre- and post-annealing data, the evaluation of retained H and D content was also performed during the annealing process. Fig. 9 combines these in-situ results (middle panel) with the previously discussed pre-annealing (left panel) and post-annealing results (right panel) for D in each sample (a)–(d). The content from the individual layers is again represented by the shades.

While the pre- and post-annealing spectra shown in Fig. 7 allowed for depth resolved quantitative data analysis, limited statistical accuracy of the data acquired during annealing introduced challenges for the quantification. On the one hand, this limitation resulted in significantly larger statistical errors during annealing. On the other hand, the limited depth resolution led to ambiguities in reproducing the spectra via simulation. Therefore, the during annealing simulations were restricted to model only surface-near contributions, while bulk contributions were omitted. This simplification can be rationalized by the fact that the out-gassing behavior during annealing was primarily governed by surface-near contributions. However, this could have lead to significant systematic errors due to the following. As mentioned in Section 2.5, we chose a primary beam that enabled utilizing a resonant cross section as given by Quillet et al. [36]. While enhancing the signal at the resonant energy, the cross-section varies largely around the resonance. Inaccurate depth profiles in the simulation thus result in the usage of incorrect cross-section values, thereby leading to erroneous quantitative results. Therefore, we want to stress that the quantitative data presented in Fig. 9 should be interpreted with caution and

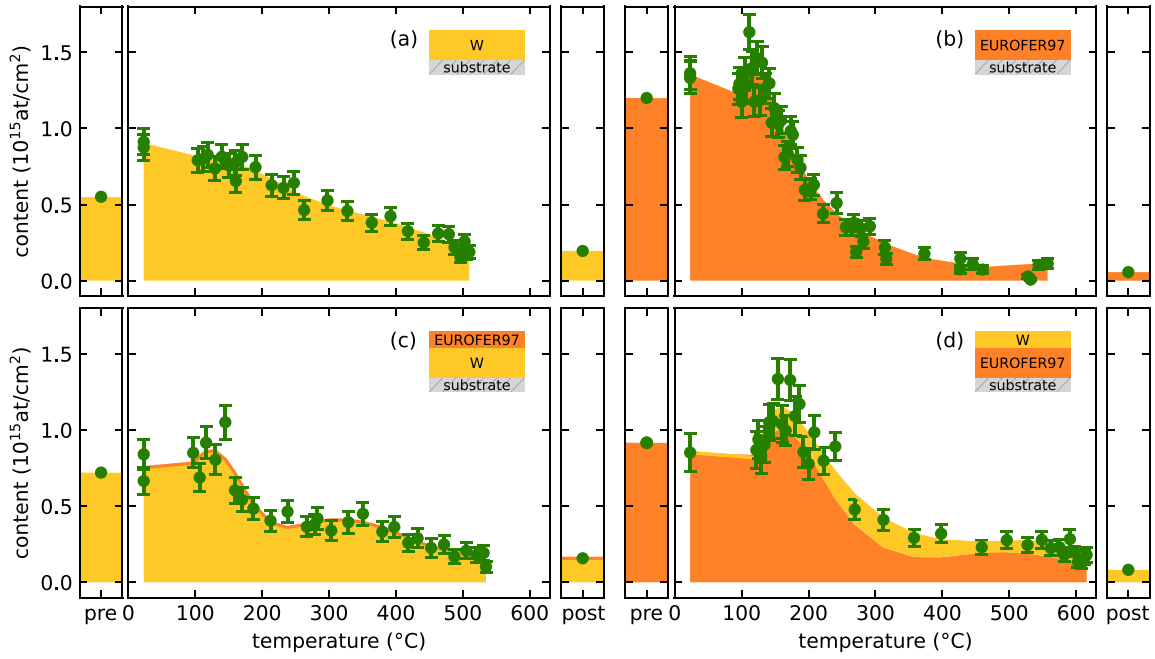

Fig. 9. Quantitative data on the retained D amount for all structures. The pre-annealing phase is shown in the box on the left, post-annealing data is shown on the right. Data obtained during the annealing procedure is shown as function of temperature in the central plot for each sample case (a)–(d). The content from the individual layers is represented by the shade. Yellow represents W, orange represents EUROFER97.

primarily serve to enable relative comparisons between the samples investigated in this study.

In agreement with previous observations, Fig. 9 shows that D contributions were progressively released with increasing annealing temperature, approaching values close to the detection limit of our system around 600 °C. Besides the overall trend of decreasing D content as function of annealing temperature from approximately 150 °C towards 600 °C, it should be noted that individual data points did not fully correspond to this decreasing trend. This restriction applied in particular to data points around 100 °C–200 °C, which corresponded to the temperature, at which high voltage was initially applied to the EBHF. This apparent slight increase in D content may have resulted from D particles diffusing from deeper regions towards the surface immediately after the onset of heating, leading to temporary accumulation in surface-near layers. The data however suggest that this diffusion from the bulk did not appear for the pure W layer (a), while all other investigated structures (b)–(d) show a more or less pronounced peak at this temperature interval. In addition, systematic errors could also have influenced this result. Firstly, the limited depth resolution and the resulting potential misestimation of the cross-section, as discussed above, may have contributed to this result. Secondly, deviations from the used cross-section data would analogously lead to wrong results. Additionally, despite the protective W foil that was installed between sample holder and sample (explained in Section 2.5), it was observed that noise from the EBHF could not be fully prevented. Therefore, influences of the initial voltage application on the detectors can also not be fully excluded. However, RBS spectra, which were recorded in parallel to ERDA did not indicate significant noise at the start of the heating ramp.

3.1. W as top layer

A distinct shift of the peak positions of the H and D peaks was observed in the ERDA spectra of the EUROFER97 + W sample, as shown in Fig. 7 (d). This effect was further analyzed by evaluating the H and D content in the different layers individually, shown by the shaded areas in Figs. 8 (d) and 9 (d). H data shown in Fig. 8 (d) indicate that the H content was reduced in both layers as a result of the annealing process. However, the situation was different for the case of D. While the orange shaded areas in Figs. 8 (d) and 9 (d), i.e. D retained in the EUROFER97 layer, were indeed decreasing steadily, the yellow shaded areas, representing the D content in the W top layer, did not show a steady decrease. As a function of temperature, the yellow shaded area, in contrast, increased at the beginning of the temperature ramp (room temperature to 150 °C) and showed a plateau at around 500 °C, before it finally decreased again when approaching 600 °C. This observation suggests that D initially implanted in EUROFER97, started to escape this layer at a certain temperature. However, instead of immediate outgassing from the surface, D remained trapped in the W layer or at the interface at this intermediate temperature until higher temperatures enabled its eventual release close to 600 °C. Comparing pre- and post-annealing, we observed that D was initially retained in the EUROFER97 layer only. The remaining D content after annealing, however, was located above the EUROFER97 layer, i.e. in the W layer or directly at the interface. This behavior suggests that redeposited W layers can function as partial barrier to D outgassing, temporarily trapping diffusing D before its eventual release at higher temperatures. Notably, this behavior was, however, not observed for the inverted layer system, thus suggesting that redeposited EUROFER97 layers did not impede D diffusion.

The observation that the layered structure EUROFER97+W shows a significantly different retention behavior compared to bare EUROFER97, while the inverted structure W+EUROFER97 does not behave differently compared to bare W, suggests that the barrier effect arises primarily from the intrinsic material properties of W and EUROFER97 rather than from the presence of an additional interface per se. Literature studies employing thermal desorption spectroscopy have shown that undamaged W exhibits a higher desorption temperature for D [37] compared to EUROFER97 [21], related to different diffusivity and solubility of hydrogen isotopes or different trapping sites in the two materials [11,38,39]. These different material properties may rationalize why the W top layer yields qualitatively different results. Furthermore, investigations by Möller et al. [20] have shown that D retention in W exceeds that in EUROFER97. Similarly, Ogorodnikova

and Sugiyama [40] reported higher retention values for damaged W compared to damaged EUROFER97 and stated that elevated temperatures are required to release T from W. While these literature reports support the trends observed within this study, we want to stress that quantitative comparisons with literature values remain challenging due to different experimental procedures, including e.g. different implantation energies and fluences, different implantation temperatures as well as different annealing temperatures. To gain a more comprehensive understanding of the mechanisms governing the observed barrier effect, further investigation through detailed microscopic modeling tailored to the specific experimental procedure could provide valuable insight.

4. Summary and conclusion

In this study, we investigated the retained D and H amount in different layer systems consisting of EUROFER97 and W. The content was quantified by IBA techniques, i.e. a combination of simultaneous RBS and ERDA, before, during and after in-situ annealing up to approximately 600 °C. Besides the IBA techniques, our experimental procedure consisted of several individual steps: Firstly, W and EUROFER97 layers were irradiated by 1 keV D_2^+ ions, leading to implantation of D in our initial layers. Subsequently, the irradiated layers were separated into two individual samples, one of which was coated with an additional layer, consisting of either EUROFER97 or W. The second sample part was kept uncoated. The final step of the experimental campaign then comprised an annealing ramp. During, before and after this annealing procedure the H and D content in the sample was monitored via IBA.

By comparing coated and uncoated samples, we found that a thin redeposited EUROFER97 layer, approximately 15–20 nm thick was practically transparent for D diffusion, resulting in the same qualitative behavior for the experimental results obtained from the non-coated W sample and the layered W + EUROFER97 structure. In contrast, samples with a redeposited W layer of similar thickness on EUROFER97 lead to reduced/delayed D outgassing. The different results found for the non-coated EUROFER97 layer and the layered system of EUROFER97 + W suggest that W functioned as outgassing barrier, hindering D diffusion.

These results highlight that simultaneous processes, such as redeposition and implantation can lead to synergistic effects, effectively resulting in different retention behaviors. This example, representing one possible scenario that can form under reactor relevant conditions, shows that a complex interplay between individual physical processes needs to be taken into account for the design and performance prediction of future nuclear fusion devices.

CRediT authorship contribution statement

Martina Fellinger: Writing – original draft, Visualization, Investigation, Formal analysis, Data curation, Conceptualization. **Eduardo Pitthan:** Writing – review & editing, Validation, Supervision, Project administration, Methodology, Investigation, Conceptualization. **Daniel Gautam:** Investigation. **Daniel Primetzhofer:** Writing – review & editing, Supervision, Resources, Project administration, Funding acquisition, Conceptualization. **Friedrich Aumayr:** Writing – review & editing, Supervision, Resources, Project administration, Funding acquisition.

Declaration of competing interest

The authors declare that they have no known competing financial interests or personal relationships that could have appeared to influence the work reported in this paper.

Acknowledgments

This work has been carried out within the framework of the EUROfusion Consortium, funded by the European Union via the Euratom Research and Training Programme (Grant Agreement No 101052200 — EUROfusion). Views and opinions expressed are however those of the author(s) only and do not necessarily reflect those of the European Union or the European Commission. Neither the European Union nor the European Commission can be held responsible for them. In addition to the EUROfusion program, financial support has also been provided by the Commission for the Coordination of Fusion Research in Austria (KKKÖ) at the Austrian Academy of Sciences (ÖAW). Support of the operation of the tandem accelerator at Uppsala University, Sweden by VR-RFI (contract #2019-00191) is gratefully acknowledged. The authors also acknowledge TU Wien Bibliothek for financial support through its Open Access Funding Programme.

Data availability

Data will be made available on request.

References

[1] V. Rohde, A. Kallenbach, V. Mertens, R. Neu, The ASDEX upgrade team, wall retention of deuterium and gaseous impurities in all tungsten ASDEX upgrade, Plasma Phys. Control. Fusion 51 (12) (2009) 124033, http://dx.doi.org/10.1088/0741-3335/51/12/124033, https://iopscience.iop.org/article/10.1088/0741-3335/51/12/124033.

[2] T. Tanabe, Review of hydrogen retention in tungsten, Phys. Scr. T159 (2014) 014044, http://dx.doi.org/10.1088/0031-8949/2014/T159/014044, https://iopscience.iop.org/article/10.1088/0031-8949/2014/T159/014044.

[3] T. Tanabe, Tritium issues to be solved for establishment of a fusion reactor, Fusion Eng. Des. 87 (5–6) (2012) 722–727, http://dx.doi.org/10.1016/j.fusengdes.2012.02.009, https://linkinghub.elsevier.com/retrieve/pii/S0920379612000646.

[4] K. Schmid, T. Schwarz-Selinger, R. Arredondo, Influence of hydrogen isotopes on displacement damage formation in EUROFER, Nucl. Mater. Energy 34 (2023) 101341, http://dx.doi.org/10.1016/j.nme.2022.101341, https://linkinghub.elsevier.com/retrieve/pii/S2352179122002228.

[5] S. Brezinsek, A. Pospieszczyk, G. Sergienko, R. Dux, M. Cavedon, M. Faitsch, K. Krieger, Chemically assisted physical sputtering of tungsten: Identification via the 6 Π to 6 Σ transition of WD in TEXTOR and ASDEX Upgrade plasmas, Nucl. Mater. Energy 18 (2019) 50–55, http://dx.doi.org/10.1016/j.nme.2018.12.004, https://linkinghub.elsevier.com/retrieve/pii/S2352179118302138.

[6] S. Brezinsek, M. Stamp, D. Nishijima, D. Borodin, S. Devaux, K. Krieger, S. Marsen, M. O'Mullane, C. Bjoerkas, A. Kirschner, JET EFDA contributors, Study of physical and chemical assisted physical sputtering of beryllium in the JET ITER-like wall, Nucl. Fusion 54 (10) (2014) 103001, http://dx.doi.org/10.1088/0029-5515/54/10/103001, https://iopscience.iop.org/article/10.1088/0029-5515/54/10/103001.

[7] K. Heinola, A. Widdowson, J. Likonen, E. Alves, A. Baron-Wiechec, N. Barradas, S. Brezinsek, N. Catarino, P. Coad, S. Koivuranta, G. Matthews, M. Mayer, P. Petersson, Fuel retention in JET ITER-Like Wall from post-mortem analysis, J. Nuclear Materials 463 (2015) 961–965, http://dx.doi.org/10.1016/j.jnucmat.2014.12.098, https://linkinghub.elsevier.com/retrieve/pii/{S0022311514010514}.

[8] S. Brezinsek, A. Kirschner, M. Mayer, A. Baron-Wiechec, I. Borodkina, D. Borodin, I. Coffey, J. Coenen, N. Den Harder, A. Eksaeva, C. Guillemaut, K. Heinola, A. Huber, V. Huber, M. Imrisek, S. Jachmich, E. Pawelec, M. Rubel, S. Krat, G. Sergienko, G. Matthews, A. Meigs, S. Wiesen, A. Widdowson, JET contributors, Erosion screening and migration of tungsten in the JET divertor, Nucl. Fusion 59 (9) (2019) 096035, http://dx.doi.org/10.1088/1741-4326/ab2aef, https://iopscience.iop.org/article/10.1088/1741-4326/ab2aef.

[9] E. Hodille, F. Ghiorghiu, Y. Addab, A. Založnik, M. Minissale, Z. Piazza, C. Martin, T. Angot, L. Gallais, M.-F. Barthe, C. Becquart, S. Markelj, J. Mougenot, C. Grisolia, R. Bisson, Retention and release of hydrogen isotopes in tungsten plasma-facing components: the role of grain boundaries and the native oxide layer from a joint experiment-simulation integrated approach, Nucl. Fusion 57 (7) (2017) 076019, http://dx.doi.org/10.1088/1741-4326/aa6d24, https://iopscience.iop.org/article/10.1088/1741-4326/aa6d24.

[10] R. Bisson, S. Markelj, O. Mourey, F. Ghiorghiu, K. Achkasov, J.-M. Layet, P. Roubin, G. Cartry, C. Grisolia, T. Angot, Dynamic fuel retention in tokamak wall materials: An in situ laboratory study of deuterium release from polycrystalline tungsten at room temperature, J. Nucl. Mater. 467 (2015) 432–438, http://dx.doi.org/10.1016/j.jnucmat.2015.07.028, https://linkinghub.elsevier.com/retrieve/pii/S0022311515301148.

[11] F. Montupet-Leblond, L. Corso, M. Payet, R. Delaporte-Mathurin, E. Bernard, Y. Charles, J. Mougenot, S. Vartanian, E. Hodille, C. Grisolia, Permeation and trapping of hydrogen in Eurofer97, Nucl. Mater. Energy 29 (2021) 101062, http://dx.doi.org/10.1016/j.nme.2021.101062, https://linkinghub.elsevier.com/retrieve/pii/S2352179121001290.

[12] O. Ogorodnikova, C. Ruset, D. Dellasega, A. Pezzoli, M. Passoni, K. Sugiyama, Y. Gasparyan, V. Efimov, Deuterium retention in dense and disordered nanostructured tungsten coatings, J. Nucl. Mater. 507 (2018) 226–240, http://dx.doi.org/10.1016/j.jnucmat.2018.04.039, https://linkinghub.elsevier.com/retrieve/pii/S0022311517314101.

[13] M. Pečovnik, S. Markelj, A. Založnik, T. Schwarz-Selinger, Influence of grain size on deuterium transport and retention in self-damaged tungsten, J. Nucl. Mater. 513 (2019) 198–208, http://dx.doi.org/10.1016/j.jnucmat.2018.10.026, https://linkinghub.elsevier.com/retrieve/pii/S0022311518307256.

[14] L. Qiao, H. Zhang, J. Xu, L. Chai, M. Hu, P. Wang, Deuterium retention and release behaviours of tungsten and deuterium co-deposited layers, J. Nucl. Mater. 502 (2018) 247–254, http://dx.doi.org/10.1016/j.jnucmat.2018.02.009, https://linkinghub.elsevier.com/retrieve/pii/S0022311517311431.

[15] A.V. Golubeva, D.I. Cherkez, Hydrogen retention in Tungsten Alloys Developed for Fusion Facilities (Review), Phys. At. Nucl. 82 (7) (2019) 996–1004, http://dx.doi.org/10.1134/{S}1063778819070068, http://link.springer.com/{10}.1134/{S1063778819070068}.

[16] P. Wang, W. Jacob, S. Elgeti, Deuterium retention in tungsten films after different heat treatments, J. Nucl. Mater. 456 (2015) 192–199, http://dx.doi.org/10.1016/j.jnucmat.2014.09.023, https://linkinghub.elsevier.com/retrieve/pii/S0022311514006138.

[17] T. Schwarz-Selinger, A critical review of experiments on deuterium retention in displacement-damaged tungsten as function of damaging dose, Mater. Res. Express 10 (10) (2023) 102002, http://dx.doi.org/10.1088/2053-1591/acfdf8, https://iopscience.iop.org/article/10.1088/2053-1591/acfdf8.

[18] Y. Oya, X. Li, M. Sato, K. Yuyama, L. Zhang, S. Kondo, T. Hinoki, Y. Hatano, H. Watanabe, N. Yoshida, T. Chikada, Thermal desorption behavior of deuterium for 6 MeV Fe ion irradiated w with various damage concentrations, J. Nucl. Mater. 461 (2015) 336–340, http://dx.doi.org/10.1016/j.jnucmat.2015.03.032, https://linkinghub.elsevier.com/retrieve/pii/S0022311515001798.

[19] G. Tynan, R. Doerner, J. Barton, R. Chen, S. Cui, M. Simmonds, Y. Wang, J. Weaver, N. Mara, S. Pathak, Deuterium retention and thermal conductivity in ion-beam displacement-damaged tungsten, Nucl. Mater. Energy 12 (2017) 164–168, http://dx.doi.org/10.1016/j.nme.2017.03.024, https://linkinghub.elsevier.com/retrieve/pii/S2352179116301053.

[20] S. Möller, R. Krug, R. Rayaprolu, B. Kuhn, E. Joußen, A. Kreter, Deuterium retention in tungsten and reduced activation steels after 3 MeV proton irradiation, Nucl. Mater. Energy 23 (2020) 100742, http://dx.doi.org/10.1016/j.nme.2020.100742, https://linkinghub.elsevier.com/retrieve/pii/S2352179120300181.

[21] A. Hollingsworth, M. Lavrentiev, R. Watkins, A. Davies, S. Davies, R. Smith, D. Mason, A. Baron-Wiechec, Z. Kollo, J. Hess, I. Jepu, J. Likonen, K. Heinola, K. Mizohata, E. Meslin, M.-F. Barthe, A. Widdowson, I. Grech, K. Abraham, E. Pender, A. McShee, Y. Martynova, M. Freisinger, A. De Backer, Comparative study of deuterium retention in irradiated eurofer and Fe–Cr from a new ion implantation materials facility, Nucl. Fusion 60 (1) (2020) 016024, http://dx.doi.org/10.1088/1741-4326/ab546e, https://iopscience.iop.org/article/10.1088/1741-4326/ab546e.

[22] J. You, R. Villari, D. Flammini, D. Marzullo, G. Mazzone, Nuclear loads and nuclear shielding performance of EU DEMO divertor: A comparative neutronics evaluation of two interim design options, Nucl. Mater. Energy 23 (2020) 100745, http://dx.doi.org/10.1016/j.nme.2020.100745, https://linkinghub.elsevier.com/retrieve/pii/S2352179120300211.

[23] G. Federici, W. Biel, M. Gilbert, R. Kemp, N. Taylor, R. Wenninger, European DEMO design strategy and consequences for materials, Nucl. Fusion 57 (9) (2017) 092002, http://dx.doi.org/10.1088/1741-4326/57/9/092002, https://iopscience.iop.org/article/10.1088/1741-4326/57/9/092002.

[24] P. Kelly, R. Arnell, Magnetron sputtering: a review of recent developments and applications, Vacuum 56 (3) (2000) 159–172, http://dx.doi.org/10.1016/S0042-207X(99)00189-X, https://linkinghub.elsevier.com/retrieve/pii/S0042207X9900189X.

[25] E. Pitthan, P. Petersson, T. Tran, D. Moldarev, R. Kaur, J. Shams-Latifi, P. Ström, M. Hans, M. Rubel, D. Primetzhofer, Thin films sputter-deposited from EUROFER97 in argon and deuterium atmosphere: Material properties and deuterium retention, Nucl. Mater. Energy 34 (2023) 101375, http://dx.doi.org/10.1016/j.nme.2023.101375, https://linkinghub.elsevier.com/retrieve/pii/S2352179123000145.

[26] P. Ström, P. Petersson, M. Rubel, G. Possnert, A combined segmented anode gas ionization chamber and time-of-flight detector for heavy ion elastic recoil detection analysis, Rev. Sci. Instrum. 87 (10) (2016) 103303, http://dx.doi.org/10.1063/1.4963709, https://pubs.aip.org/rsi/article/87/10/103303/368409/A-combined-segmented-anode-gas-ionization-chamber.

[27] K. Kantre, M. Moro, D. Moldarev, D. Johansson, D. Wessman, M. Wolff, D. Primetzhofer, SIGMA: A Set-up for In-situ Growth, Material modification and Analysis by ion beams, Nucl. Instrum. Methods Phys. Res. Sect. B: Beam Interactions Mater. Atoms 463 (2020) 96–100, http://dx.doi.org/10.1016/j.nimb.2019.11.007, https://linkinghub.elsevier.com/retrieve/pii/S0168583X19307621.

[28] J. Brötzner, C. Cupak, M. Fellinger, H. Biber, A. Lopez-Cazalilla, F. Granberg, F. Kporha, A. Mutzke, R. González-Arrabal, F. Aumayr, Sputtering yield reduction for nano-columnar w surfaces under d ion irradiation, Nucl. Mater. Energy 37 (2023) 101507, http://dx.doi.org/10.1016/j.nme.2023.101507, https://linkinghub.elsevier.com/retrieve/pii/S2352179123001461.

[29] A. Mutzke, R. Schneider, W. Eckstein, R. Dohmen, K. Schmid, U. Von Toussaint, G. Bandelow, IPP-Report, 2019, SDTrimSP Version 6.00.

[30] P. Szabo, D. Weichselbaum, H. Biber, C. Cupak, A. Mutzke, R. Wilhelm, F. Aumayr, Graphical user interface for SDTrimSP to simulate sputtering, ion implantation and the dynamic effects of ion irradiation, Nucl. Instrum. Methods Phys. Res. Sect. B: Beam Interactions Mater. Atoms 522 (2022) 47–53, http://dx.doi.org/10.1016/j.nimb.2022.04.008, https://linkinghub.elsevier.com/retrieve/pii/{S0168583}X22001069.

[31] M. Mayer, SIMNRA, a simulation program for the analysis of NRA, RBS and ERDA, in: AIP Conference Proceedings, AIP, Denton, Texas (USA, 1999, pp. 541–544, http://dx.doi.org/10.1063/1.59188, https://pubs.aip.org/aip/acp/article/475/1/541-544/953322.

[32] D. Naujoks, J. Roth, K. Krieger, G. Lieder, M. Laux, Erosion and redeposition in the ASDEX Upgrade divertor, J. Nucl. Mater. 210 (1–2) (1994) 43–50, http://dx.doi.org/10.1016/0022-3115(94)90221-6, https://linkinghub.elsevier.com/retrieve/pii/0022311594902216.

[33] M. Ialovega, C. Martin, C. Pardanaud, E. Bernard, M. Cabié, A. Campos, C. Grisolia, M. Minissale, T. Neisius, T. Angot, R. Bisson, Deuterium retention in tungsten oxide: the role of oxide damage, Nucl. Fusion 65 (7) (2025) 076024, http://dx.doi.org/10.1088/1741-4326/addfea, https://iopscience.iop.org/article/10.1088/1741-4326/addfea.

[34] E. Pitthan, M. Moro, S. Corrêa, D. Primetzhofer, Assessing boron quantification and depth profiling of different boride materials using ion beams, Surf. Coat. Technol. 417 (2021) 127188, http://dx.doi.org/10.1016/j.surfcoat.2021.127188, https://linkinghub.elsevier.com/retrieve/pii/S0257897221003625.

[35] P. Ström, D. Primetzhofer, Ion beam tools for nondestructive in-situ and in-operando composition analysis and modification of materials at the tandem Laboratory in uppsala, J. Instrum. 17 (04) (2022) P04011, http://dx.doi.org/10.1088/1748-0221/17/04/P04011, https://iopscience.iop.org/article/10.1088/1748-0221/17/04/P04011.

[36] V. Quillet, F. Abel, M. Schott, Absolute cross section measurements for h and d elastic recoil using 1 to 2.5 MeV 4He ions, and for the 12C(d, p) 13C and 160(d, p,) 170 nuclear reactions, Nucl. Instrum. Methods Phys. Res. Sect. B: Beam Interactions Mater. Atoms 83 (1–2) (1993) 47–61.

[37] Y. Gasparyan, O. Ogorodnikova, V. Efimov, A. Mednikov, E. Marenkov, A. Pisarev, S. Markelj, I. Čadež, Thermal desorption from self-damaged tungsten exposed to deuterium atoms, J. Nucl. Mater. 463 (2015) 1013–1016, http://dx.doi.org/10.1016/j.jnucmat.2014.11.022, https://linkinghub.elsevier.com/retrieve/pii/S0022311514008137.

[38] F. Liu, H. Zhou, X.-C. Li, Y. Xu, Z. An, H. Mao, W. Xing, Q. Hou, G.-N. Luo, Deuterium gas-driven permeation and subsequent retention in rolled tungsten foils, J. Nucl. Mater. 455 (1–3) (2014) 248–252, http://dx.doi.org/10.1016/j.jnucmat.2014.06.005, https://linkinghub.elsevier.com/retrieve/pii/S0022311514003626.

[39] R. Frauenfelder, Solution and diffusion of Hydrogen in Tungsten, J. Vac. Sci. Technol. 6 (3) (1969) 388–397, http://dx.doi.org/10.1116/1.1492699, https://pubs.aip.org/jvst/article/6/3/388/249103/Solution-and-Diffusion-of-Hydrogen-in-Tungsten.

[40] O. Ogorodnikova, K. Sugiyama, Effect of radiation-induced damage on deuterium retention in tungsten, tungsten coatings and eurofer, J. Nucl. Mater. 442 (1–3) (2013) 518–527, http://dx.doi.org/10.1016/j.jnucmat.2013.07.024, https://linkinghub.elsevier.com/retrieve/pii/S0022311513009124.